Article

Lense–Thirring precessing magnetar engine drives a superluminous supernova

https://doi.org/10.1038/s41586-026-10151-0

Received: 16 July 2025

Accepted: 16 January 2026

Published online: 11 March 2026

Check for updates

Joseph R. Farah[1,2]✉, Logan J. Prust[3,4,11], D. Andrew Howell[1,2,11], Yuan Qi Ni[1,3,11], Curtis McCully[1], Moira Andrews[1,2], Harsh Kumar[5,6], Daichi Hiramatsu[5,6,7], Sebastian Gomez[5,8], Kathryn Wynn[1,2], Alexei V. Filippenko[9], K. Azalee Bostroem[10], Edo Berger[5,6] & Peter Blanchard[5,6]

Type I superluminous supernovae (SLSNe-I) are at least an order of magnitude brighter than standard SNe, with the power source for their luminosity still unknown[1–3]. The central engines of SLSNe-I are suggested to be magnetars[4,5] but most of the SLSNe-I light curves have several bumps that are unexplained by the standard magnetar model[6–8]. Existing explanations for the bumps either modulate the engine luminosity or invoke interactions with circumstellar material (CSM). Surveys of the limited sample of SLSN-I light curves find no compelling evidence favouring either scenario[7,9], leaving both the nature of the light-curve fluctuations and the applicability of the magnetar model unresolved. Here we report high-cadence multiband observations of a SLSN-I with clear 'chirped' (that is, decreasing period) light-curve bumps that can be directly linked to the properties of the magnetar central engine. Our observations are consistent with a magnetar centrally located within the expanding supernova ejecta, surrounded by an infalling accretion disk undergoing Lense–Thirring precession. Our analysis demonstrates that the light curve and bump frequency independently and self-consistently constrain the magnetar spin period to $P = 4.2 \pm 0.2$ ms and the magnetic-field strength to $B = (1.6 \pm 0.1) \times 10^{14}$ G. These results provide the first observational evidence of the Lense–Thirring effect in the environment of a magnetar and confirm the magnetar spin-down model as an explanation for the extreme luminosity observed in SLSNe-I. We anticipate that this discovery will create avenues for testing general relativity in a new regime—the violent centres of young SNe.

Supernova (SN) 2024afav is a nearby (approximately 327 Mpc) SLSN-I that showed the first unambiguously chirped light-curve modulations ever observed in a SN. It was discovered by the Liverpool–Gravitational-wave Optical Transient Observer (L-GOTO) collaboration on 12 December 2024 (all times in UTC (ref. 10)) and classified by the extended Public European Southern Observatory Spectroscopic Survey of Transient Objects (ePESSTO+) collaboration as a SLSN-I on 24 January 2025 (ref. 11) based on spectral features (see also Extended Data Fig. 1). Early observations indicated an exponential roughly 40-day rise followed by a bumpy, approximately 50-day quasi-plateau phase peaking at absolute magnitude about −20.5 (Fig. 1). Part-way through the 'plateau', we triggered observations using the Las Cumbres Observatory (LCO) through the Global Supernova Project (GSP) and the Fred Lawrence Whipple Observatory (FLWO) KeplerCam to obtain photometry and spectra (see Methods section 'Observations and data reduction' for a full discussion). Following the appearance of a second (Modified Julian Date (MJD) 60736) and third (MJD 60779) sinusoidal modulation in the light curve, each with a period reduced by about 35%, we phenomenologically predicted both the epochs and luminosities of subsequent bumps and dynamically adjusted our observation campaign to capture them (Methods section 'Observations and data reduction'). In this way, we successfully observed a fourth (MJD 60802) and a possible fifth (MJD 60820) modulation, refining the initial period reduction fraction estimate to about 29 ± 10% (Methods section 'Residual analysis').

In the prevailing theory to explain SLSNe, a strongly magnetized millisecond pulsar (magnetar) is created in the SN explosion. As the magnetar emits energy by means of magnetic dipole radiation, the spin rate decreases and it transfers some of this energy to the expanding ejecta[4,5]. However, although initial analytic models determined that the energy budgets were sufficient to power the SLSN, they did not investigate a mechanism of energy transfer.

The magnetar model predicts a rapid rise followed by a smooth, monotonic decline. Despite the magnetar model predicting smooth monotonic behaviour in the light curve post-peak, most SLSNe-I are observed to have bumps or modulations of some kind[6–8]. In the context of a magnetar-powered model, previous studies have attempted to explain light-curve fluctuations in SLSNe-I by invoking either aperiodic (for example, magnetar flares[12]) or completely periodic (for example, misaligned magnetic inclination angle precession[13]) modulations of the central engine, which have been successfully modelled against light

[1]Las Cumbres Observatory, Goleta, CA, USA. [2]Department of Physics, University of California, Santa Barbara, Santa Barbara, CA, USA. [3]Kavli Institute for Theoretical Physics, Santa Barbara, CA, USA. [4]Center for Computational Astrophysics, Flatiron Institute, New York, NY, USA. [5]Center for Astrophysics | Harvard & Smithsonian, Cambridge, MA, USA. [6]The NSF AI Institute for Artificial Intelligence and Fundamental Interactions (IAIFI), Cambridge, MA, USA. [7]Department of Astronomy, University of Florida, Gainesville, FL, USA. [8]Department of Astronomy, The University of Texas at Austin, Austin, TX, USA. [9]Department of Astronomy, University of California, Berkeley, Berkeley, CA, USA. [10]Steward Observatory, University of Arizona, Tucson, AZ, USA. [11]These authors contributed equally: Logan J. Prust, D. Andrew Howell, Yuan Qi Ni. ✉e-mail: jfarah@lco.global

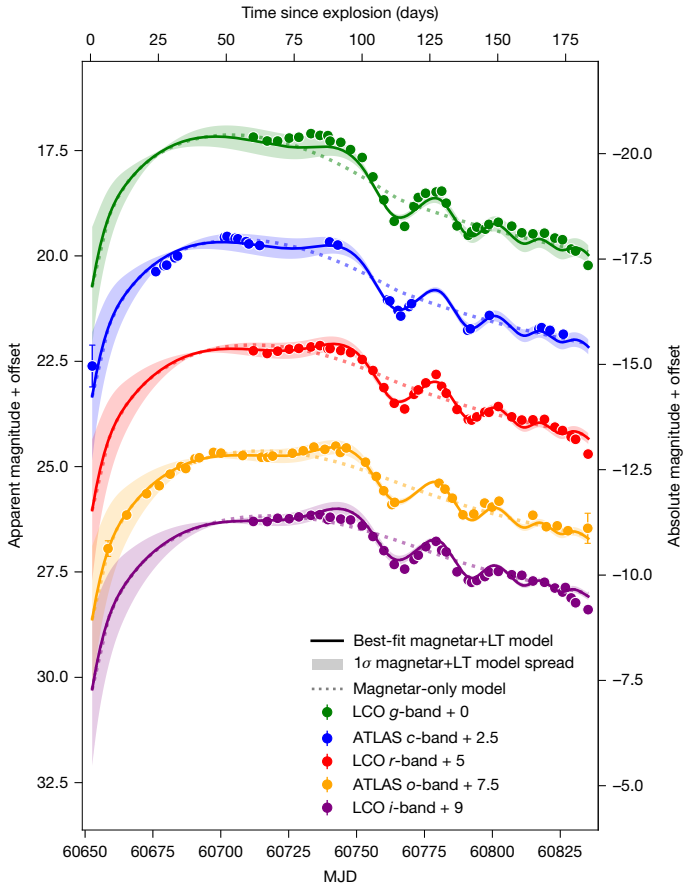

Fig. 1 | Multiband light curves of SN 2024afav. The combined LCO + ATLAS + KeplerCam light curves of SN 2024afav, from shortly after explosion to about 125 days post-peak. Error bars represent 1σ uncertainties computed from the photometry and may be smaller than the data points. The magnetar model is shown as the dotted line ('magnetar-only'; Methods section 'Magnetar-only model fits'). Although the data on average are consistent with the magnetar model, there is a chirped signal post-peak that the model fails to explain. We model the light curve as generated by an infalling accretion disk undergoing Lense–Thirring precession ('magnetar+LT'; solid line; Methods section 'Construction and fit of the Lense–Thirring modulation model'; $k = 15$ model degrees of freedom) and find that the model reproduces the overall behaviour of the data, with reduced $\chi^2 \approx 1.5$ for the whole fit ($N = 706$ data points) and reduced $\chi^2 \approx 1.6$ for the modulations (40–180 days, $N = 618$ data points).

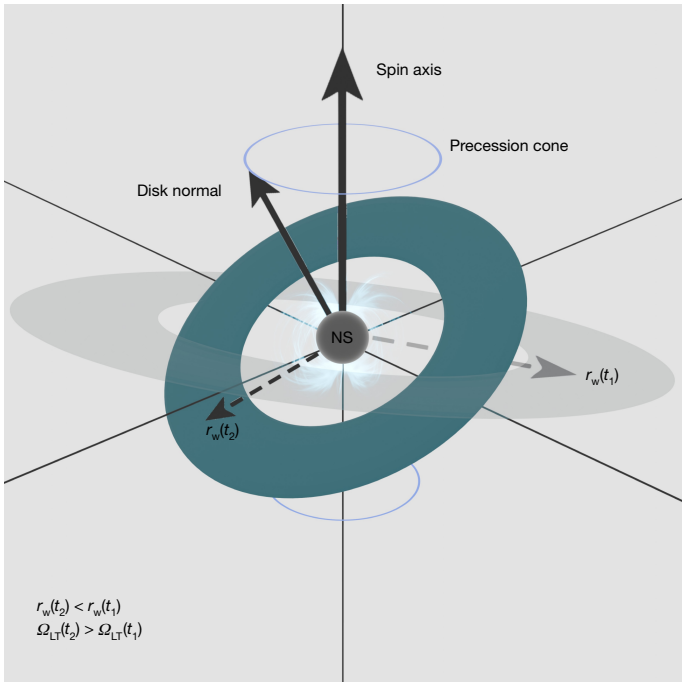

Fig. 2 | Diagram of disk infall and precession. Schematic diagram showing the physical picture motivating the magnetar+LT model. The magnetar is shown in the centre of the grid (grey sphere, NS), producing emission that is modulated along the observer's line of sight by an accretion disk (blue annulus). The misalignment between the accretion disk and the spin axis of the neutron star induces a Lense–Thirring torque that causes the disk to precess (with frequency $\Omega_{LT} \propto r^{-3}$) around the spin axis, producing modulations in the light curve from the perspective of the observer as the disk periodically blocks or reflects the spin-down energy from the magnetar. As the accretion disk infalls from a larger radius $r_w(t_1)$ (grey annulus) to a smaller one $r_w(t_2)$ (blue annulus), the induced Lense–Thirring torque increases and the precession (and therefore modulation frequency) increases as well.

curves with ≤2 bumps. The standard magnetar model fails to explain the unusual chirped signal in SN 2024afav, as shown in Fig. 1 (see also Extended Data Fig. 2). Although some bumps are common in SLSN-I light curves[7], existing models are fundamentally incompatible with a light curve with ≥4 unambiguous modulations showing a decaying period.

The appearance of a clear, damped, quasi-periodic component of the light curve motivates exploration of a physical mechanism that may be able to explain the timing of the modulations. A young magnetar in certain circumstances may form a small, tilted (relative to the magnetar spin axis) accretion disk from matter originating in the progenitor star that failed to eject during the SN (Fig. 2; Methods section 'Construction and fit of the Lense–Thirring modulation model')[14–16]. The radius of the misaligned disk is set by the equilibrium between the radiation pressure from the magnetar-launched wind and the ram pressure of the disk[17,18], which shifts inward as the accretion rate decreases, leading to the disk 'infall' (Supplementary Information Section 2). Any misalignment between the accretion disk and the spin axis of the neutron star would induce a Lense–Thirring torque on the accretion disk (see, for example, refs. 19–23 for a review), causing it to precess (with increasing frequency owing to the infall) around the magnetar spin axis. As the accretion disk precesses, it may periodically modulate the emission from the magnetar by, for example, alternately obscuring or reflecting the magnetar luminosity (as in, for example, refs. 24,25), redirecting a jet[26,27] along the normal of the accretion disk (as in, for example, ref. 28), redirecting wind from the disk itself (as in, for example, ref. 29) or changing the accretion rate onto the magnetar[30]. The modulating emission from the magnetar could lead to a non-constant deposition of energy in the SN ejecta (for example, ref. 13) that precesses with the accretion disk and appears to an observer to oscillate on the Lense–Thirring timescale of $P_{LT} \approx 25$–45 days (Methods section 'Construction and fit of the Lense–Thirring modulation model'). High-energy photons from the magnetar interact with the ejecta and are reprocessed into optical photons, delaying the emission and diffusing out on a timescale of $t_d \approx 15$ days during the bumps[31,32] (see also Methods section 'Construction and fit of the Lense–Thirring modulation model'). The intensity of the bumps is determined not only by the energy injection[29,33] but also the reprocessing and diffusion characteristics of the expanding ejecta[34]. However, the evolving periodicity of the modulations is solely determined by the properties of the precession (Methods section 'Construction and fit of the Lense–Thirring modulation model'), enabling a direct examination of strong-gravity effects in the vicinity of the magnetar. For our analysis, we propose a phenomenological model composed of a sinusoid acting on a Lense–Thirring precession phase function, modulated by a Gaussian envelope to match the observations. These modulations are added directly to the magnetar model.

We fit our combined magnetar and Lense–Thirring precession model to the SN 2024afav light curve (labelled 'magnetar+LT' in Fig. 1).

Crucially, the phase component of the modulation has only two free parameters—the initial phase of the accretion disk and the accretion rate—and is otherwise entirely determined by the parameters of the magnetar (Methods section 'Construction and fit of the Lense–Thirring modulation model'). We find that our model reproduces the overall behaviour of the transient during both the rise and the modulations (reduced $\chi^2 \approx 1.5$ for the whole fit, reduced $\chi^2 \approx 1.6$ for the modulations; Methods section 'Construction and fit of the Lense–Thirring modulation model'). Assuming standard neutron star mass ($M_{NS} \approx 1.4\ M_\odot$) and size ($R_{NS} \approx 10^6$ cm), we can separately constrain the magnetar spin period P using the observed rise to peak (spin-down energy injection constraint) and the residual behaviour of the modulations (Lense–Thirring precession constraint). We find that the periods determined from the rise in the standard magnetar model ($P = 5.5 \pm 1.25$ ms; Methods section 'Magnetar-only model fits') and the modulations ($P = 5.4 \pm 1.8$ ms; Supplementary Information Section 2) are statistically self-consistent and, combined with the estimate from the full light curve (forward-modelling both the magnetar model and Lense–Thirring precession-driven modulation model simultaneously), constrain the spin of the magnetar to $P = 4.2 \pm 0.2$ ms (Methods section 'Construction and fit of the Lense–Thirring modulation model'). Such self-consistency is notable, as it suggests that the modulations and overall light-curve behaviour can be directly derived from the same properties of the magnetar. Similarly, combining the measurements from the early light curve and the modulations, the magnetic-field strength is constrained to be $B \approx (1.6 \pm 0.1) \times 10^{14}$ G (Methods section 'Construction and fit of the Lense–Thirring modulation model'). Assuming that the accretion disk is wind-supported[17,18], we constrain the accretion rate to $\dot{M}(t = 30\ \text{days}) = \dot{M}_0 = (3.71 \pm 0.36) \times 10^{-5}\ M_\odot$ per year (Supplementary Information Section 2).

We consider alternative physical scenarios that may produce the same oscillating light-curve behaviour, including various kinds of precession and input energy modulation (Supplementary Information Section 3). Existing explanations that invoke a precession-driven magnetic inclination angle variations of a deformed magnetar predict approximately the correct timescale for the modulations[13] but a positive precession period derivative as the magnetar spins down, contrasting with the observations, which show a decreasing period. With the assumption that a precessing accretion disk is instead modulating the line-of-sight energy injection from the magnetar into the ejecta, we consider alternative origins of the precession. Apsidal precession is unlikely, as the disk is highly circularized within minutes to hours of formation[35]. Magnetic warp precession[36] and quadrupole-driven nodal precession[37–39] can give comparable periodicities. However, neither can produce the required period derivative and, in the case of magnetic warp precession, the period is expected to increase owing to an induced disk-threading torque[36]. By contrast, the tilted, infalling accretion disk undergoing Lense–Thirring precession gives the correct timescales and precession period derivative without deviating from the properties of the magnetar inferred from the overall behaviour of the SN (Fig. 3).

Some explanations of modulations in SLSN-I light curves have proposed interaction with CSM as the origin (for example, refs. 7,40,41). In particular, the modulations in SN 2017egm were found to favour a CSM interaction origin over alternative scenarios[41]. The scenario of ref. 41 could be used to model arbitrary modulations in a SLSN-I light curve, including SN 2024afav. However, we consider the CSM modulation mechanism less likely for several reasons. First, to reproduce ≥4 modulations with decaying period and amplitude requires dozens of highly fine-tuned CSM parameters. Second, the shape of the modulation is firmly sinusoidal, as is visible in the residuals (Extended Data Fig. 3), contrasting with the more irregular shape produced by the CSM model of ref. 40. Third, the light curve has no modulations until well beyond the diffusion timescale ($t_d \gtrsim 37$ days), consistent with a central-engine-based mechanism. Finally, our proposed description of the oscillating behaviour in SN 2024afav sees its goodness of fit improve when a diffusion correction with no more free parameters is incorporated (Methods section 'Construction and fit of the Lense–Thirring modulation model'), behaviour that has been used to favour a central-engine origin over CSM interaction[7]. Thus, interaction with CSM is unlikely to be the origin of the observed light-curve modulations in SN 2024afav. However, this does not preclude CSM interactions from being present at a lower level. We investigate this possibility further in ref. 42.

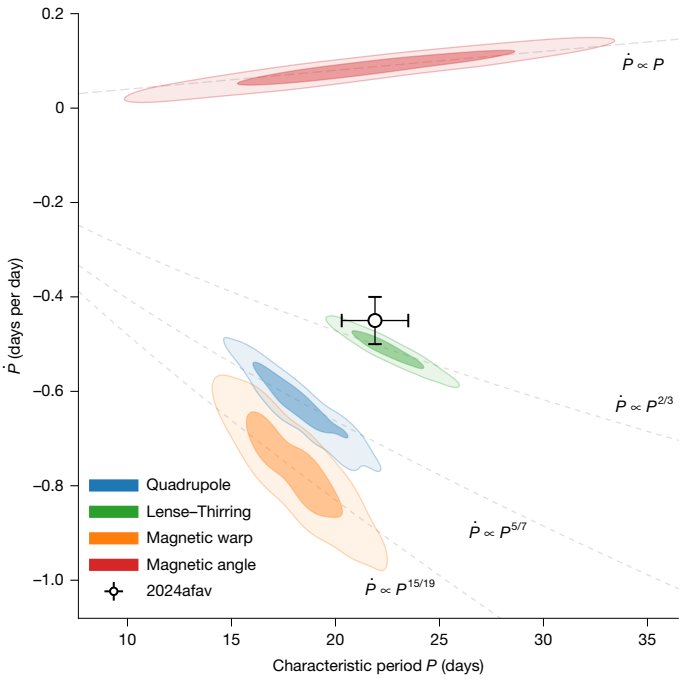

Fig. 3 | Alternative explanations of modulations. Ability of alternative scenarios to explain the modulation of the SN 2024afav light curve. We analyse other possible origins of the accretion-disk precession to assess the uniqueness of the ability of the Lense–Thirring model to explain the observed modulations in SN 2024afav. We characterize the candidate explanations based on their characteristic period (average period over the 80 days when the bumps are visible) and precession-period derivative (Supplementary Information Section 3). The corresponding location of SN 2024afav is shown as the point with error bars. 1σ and 2σ contours are shown for the candidate explanations based on the MOSFiT uncertainties (Methods section 'Magnetar-only model fits'). For models not equipped with an $\dot{\Omega} > 0$ behaviour, we invoked radial infall to explain the changing period. We consider magnetic-angle precession, quadrupole-driven nodal precession and magnetic-warp precession. Only the Lense–Thirring effect around a magnetar produces a characteristic period and period derivative consistent with the observations. Dashed grey lines indicate the predicted $\dot{P}(P)$ behaviour based on the linear radial infall assumption described in Methods section 'Construction and fit of the Lense–Thirring modulation model'.

The uniquely high cadence (about 0.5 days) and extended (about 200 days) quality of our dataset unambiguously reveal chirped modulations in a SLSN-I light curve, behaviour that is evidence of a central-engine origin. Moreover, both the overall light-curve evolution and the modulations themselves are quantitatively consistent with a magnetar-powered model, confirming its viability as an explanation for the extreme luminosity of SLSNe-I and providing evidence of a direct physical mechanism to communicate the magnetar spin-down power into the ejecta. Our analysis further demonstrates that Lense–Thirring precession provides the most plausible explanation for the chirped signal, constituting observational evidence of the Lense–Thirring effect in a magnetar and establishing the influence of general relativistic frame-dragging in a new astrophysical regime: young SNe.

We also find that our framework reproduces the behaviour of previously observed SLSNe-I with periodic light-curve features

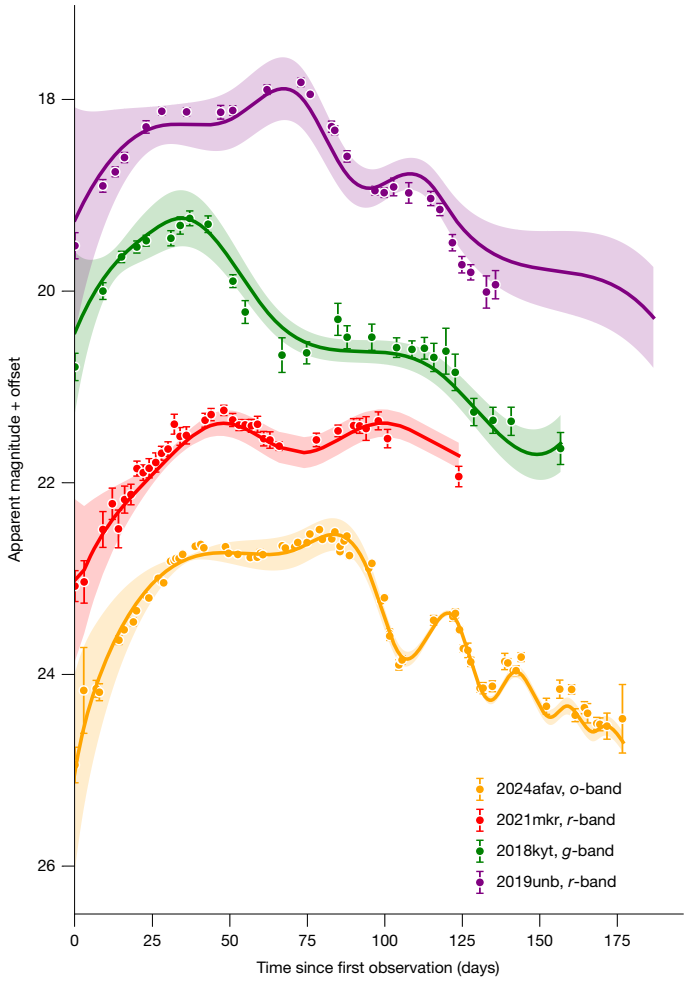

Fig. 4 | Application to legacy SLSNe-I. Fits to other SLSNe-I using the magnetar+LT model. Periodic fluctuations (with ≤2 bumps observed) in SN 2018kyt (green), SN 2019unb (purple) and SN 2021mkr (red) were explained using CSM interaction, magnetic-inclination precession or central-engine flares. These solutions are either periodic on the timescale of the SN or aperiodic and cannot describe the chirped behaviour of SN 2024afav (orange). By contrast, we find that the magnetar+LT model can explain the behaviour in these other objects as well as SN 2024afav. (Note: bands for each object were selected on the basis of which band most clearly showed the modulations. Error bars represent 1σ uncertainties from the photometry and may be smaller than the data points).

(Supplementary Information Section 4). Previous extensions of the magnetar model[12,13,41,43] to explain periodic behaviour fail to reproduce the rapidly decaying period we observe in SN 2024afav; by contrast, our model can accommodate both chirped behaviour as well as the completely periodic behaviour observed in some SLSNe-I. We consider a sample of SLSNe-I that have been modelled previously using CSM interaction (SN 2019unb (refs. 7,8)), central-engine flares (SN 2021mkr (ref. 12)) and magnetar precession (SN 2018kyt (ref. 13)). We find that these objects can be satisfactorily modelled using our magnetar+LT model (Fig. 4). For each source, the observed period follows directly from the best-fit magnetar spin and magnetic-field strength, which fix the Lense–Thirring torque and hence the precession frequency (Methods section 'Construction and fit of the Lense–Thirring modulation model' and Supplementary Information Section 4). Thus, SLSNe described by three different mutually inconsistent physical mechanisms can now be described by one.

Forthcoming wide-field surveys, particularly the Legacy Survey of Space and Time (LSST)[44,45], are expected to discover thousands to tens of thousands of SLSNe-I (ref. 46), which may be followed with facilities such as the LCO to acquire the extended observations needed to detect the fainter modulations predicted by the magnetar+LT model. This sample would provide a powerful test bed for the magnetar model and enable population-level inference of magnetar properties. Detailed follow-up campaigns will lead to robust constraints on magnetar properties and—when combined with spectral diagnostics of accretion and ejecta—possibly even tests of general relativity using infant magnetars.

Online content

Any methods, additional references, Nature Portfolio reporting summaries, source data, extended data, supplementary information, acknowledgements, peer review information; details of author contributions and competing interests; and statements of data and code availability are available at https://doi.org/10.1038/s41586-026-10151-0.

1. Gal-Yam, A. in *Handbook of Supernovae* (eds Alsabti, A. W. & Murdin, P.) 195–237 (Springer, 2017).
2. Moriya, T. J., Sorokina, E. I. & Chevalier, R. A. Superluminous supernovae. In *Supernovae* (eds Bykov, A. et al.) Vol. 68, 109–145 (Springer, 2019).
3. Quimby, R. Superluminous supernovae. *Zenodo* https://doi.org/10.5281/zenodo.3478147 (2019).
4. Kasen, D. & Bildsten, L. Supernova light curves powered by young magnetars. *Astrophys. J.* **717**, 245–249 (2010).
5. Woosley, S. E. Bright supernovae from magnetar birth. *Astrophys. J. Lett.* **719**, L204–L207 (2010).
6. Lunnan, R. et al. Hydrogen-poor superluminous supernovae from the Pan-STARRS1 Medium Deep Survey. *Astrophys. J.* **852**, 81 (2018).
7. Hosseinzadeh, G. et al. Bumpy declining light curves are common in hydrogen-poor superluminous supernovae. *Astrophys. J.* **933**, 14 (2022).
8. Chen, Z. H. et al. The hydrogen-poor superluminous supernovae from the Zwicky Transient Facility Phase I survey. II. Light-curve modeling and characterization of undulations. *Astrophys. J.* **943**, 42 (2023).
9. Chatzopoulos, E. & Tuminello, R. A systematic study of superluminous supernova light-curve models using clustering. *Astrophys. J.* **874**, 68 (2019).
10. Kumar, A. et al. GOTO Transient Discovery Report for 2024-12-27. Transient Name Server Discovery Report, No. 2024-5091 (2024).
11. de Wet, S., Wichern, H., Leloudas, G. & Yaron, O. ePESSTO+ Transient Classification Report for 2025-01-24. Transient Name Server Classification Report, No. 2025-337 (2025).
12. Dong, X.-F., Liu, L.-D., Gao, H. & Yang, S. Magnetar flare-driven bumpy declining light curves in hydrogen-poor superluminous supernovae. *Astrophys. J.* **951**, 61 (2023).
13. Zhang, B., Li, L., Dai, Z.-G. & Zhong, S.-Q. Hydrogen-poor superluminous supernovae with bumpy light curves powered by precessing magnetars. *Astrophys. J.* **985**, 172 (2025).
14. Ogilvie, G. I. & Dubus, G. Precessing warped accretion discs in X-ray binaries. *Mon. Not. R. Astron. Soc.* **320**, 485–503 (2001).
15. Perna, R., Duffell, P., Cantiello, M. & MacFadyen, A. I. The fate of fallback matter around newly born compact objects. *Astrophys. J.* **781**, 119 (2014).
16. Lin, W., Wang, X., Wang, L. & Dai, Z. Supernova luminosity powered by magnetar–disk system. *Astrophys. J. Lett.* **914**, L2 (2021).
17. Chashkina, A., Lipunova, G., Abolmasov, P. & Poutanen, J. Super-Eddington accretion discs with advection and outflows around magnetized neutron stars. *Astron. Astrophys.* **626**, A18 (2019).
18. Tamilan, M., Hayasaki, K. & Suzuki, T. K. Steady-state solutions for a geometrically thin accretion disk with magnetically driven winds. *Prog. Theor. Exp. Phys.* **2025**, 023E02 (2025).
19. Mashhoon, B., Hehl, F. W. & Theiss, D. S. On the gravitational effects of rotating masses: the Thirring-Lense papers. *Gen. Relativ. Gravit.* **16**, 711–750 (1984).
20. Iorio, L. *General Post-Newtonian Orbital Effects: From Earth's Satellites to the Galactic Centre* (Cambridge Univ. Press, 2024).
21. Iorio, L. Lense-Thirring effect at work in M87*. *Phys. Rev. D* **111**, 044035 (2025).
22. Iorio, L., Lichtenegger, H. I. M., Ruggiero, M. L. & Corda, C. Phenomenology of the Lense-Thirring effect in the solar system. *Astrophys. Space Sci.* **331**, 351–395 (2011).
23. Renzetti, G. History of the attempts to measure orbital frame-dragging with artificial satellites. *Cent. Eur. J. Phys.* **11**, 531–544 (2013).
24. Jurua, E., Charles, P. A., Still, M. & Meintjes, P. J. The optical and X-ray light curves of Hercules X-1. *Mon. Not. R. Astron. Soc.* **418**, 437–443 (2011).
25. Romanova, M. M. et al. MHD Simulations of Magnetospheric Accretion, Ejection and Plasma-field Interaction. In *Proc. European Physical Journal Web of Conferences*, Vol. 64, 05001 (EDP Sciences, 2014).
26. Soker, N. Jets launched at magnetar birth cannot be ignored. *New Astron.* **47**, 88–90 (2016).
27. Bucciantini, N., Quataert, E., Arons, J., Metzger, B. D. & Thompson, T. A. Relativistic jets and long-duration gamma-ray bursts from the birth of magnetars. *Mon. Not. R. Astron. Soc.* **383**, L25–L29 (2008).
28. Liska, M. et al. Formation of precessing jets by tilted black hole discs in 3D general relativistic MHD simulations. *Mon. Not. R. Astron. Soc.* **474**, L81–L85 (2018).
29. Dexter, J. & Kasen, D. Supernova light curves powered by fallback accretion. *Astrophys. J.* **772**, 30 (2013).

30. Nixon, C., King, A., Price, D. & Frank, J. Tearing up the disk: how black holes accrete. *Astrophys. J. Lett.* **757**, L24 (2012).
31. Rybicki, G. B. & Lightman, A. P. *Radiative Processes in Astrophysics* (Wiley, 1986).
32. Sonneborn, G. et al. X-ray Heating Of The Ejecta Of Supernova 1987A. In *Proc. 219th American Astronomical Society Meeting Abstracts*, 242.25 (American Astronomical Society, 2012).
33. Menou, K., Perna, R. & Hernquist, L. Stability and evolution of supernova fallback disks. *Astrophys. J.* **559**, 1032–1046 (2001).
34. Arnett, W. D. Type I supernovae. I - Analytic solutions for the early part of the light curve. *Astrophys. J.* **253**, 785–797 (1982).
35. Armitage, P. J. Eccentricity of masing disks in Active Galactic Nuclei. Preprint at https://arxiv.org/abs/0802.1524 (2008).
36. Lai, D. Magnetically driven warping, precession, and resonances in accretion disks. *Astrophys. J.* **524**, 1030–1047 (1999).
37. Morsink, S. M. & Stella, L. Relativistic precession around rotating neutron stars: effects due to frame dragging and stellar oblateness. *Astrophys. J.* **513**, 827–844 (1999).
38. Colaiuda, A., Ferrari, V., Gualtieri, L. & Pons, J. A. Relativistic models of magnetars: structure and deformations. *Mon. Not. R. Astron. Soc.* **385**, 2080–2096 (2008).
39. Tremaine, S. & Davis, S. W. Dynamics of warped accretion discs. *Mon. Not. R. Astron. Soc.* **441**, 1408–1434 (2014).
40. Liu, L.-D., Wang, L.-J., Wang, S.-Q. & Dai, Z.-G. A multiple ejecta-circumstellar medium interaction model and its implications for superluminous supernovae iPTF15esb and iPTF13dcc. *Astrophys. J.* **856**, 59 (2018).
41. Lin, W. et al. A superluminous supernova lightened by collisions with pulsational pair-instability shells. *Nat. Astron.* **7**, 779–789 (2023).
42. Kumar, H. et al. SN 2024afav: A superluminous supernova with multiple light-curve bumps and spectroscopic signatures of circumstellar interaction. *Astrophys. J. Lett.* **998**, L3 (2026).
43. West, S. L. et al. SN 2020qlb: a hydrogen-poor superluminous supernova with well-characterized light curve undulations. *Astron. Astrophys.* **670**, A7 (2023).
44. Ivezić, Ž et al. LSST: from science drivers to reference design and anticipated data products. *Astrophys. J.* **873**, 111 (2019).
45. Tyson, J. A. Large Synoptic Survey Telescope: Overview. In *Survey and Other Telescope Technologies and Discoveries*, Vol. 4836, 10–20 (SPIE, 2002).
46. Villar, V. A., Nicholl, M. & Berger, E. Superluminous supernovae in LSST: rates, detection metrics, and light-curve modeling. *Astrophys. J.* **869**, 166 (2018).

Methods

Observations and data reduction

SN 2024afav is located at right ascension 12 h 49 min 12.050 s and declination −18° 06′ 12.61″ (J2000 epoch), in the vicinity of the faint galaxy GALEXASC J124911.85-180609.6. The unusually bright absolute magnitude (about −20.5 in the *g*-band at peak, *K*-correction of $K = -0.06$ (ref. 47)) and a hydrogen-deficient spectrum led to a classification by the ePESSTO+ in January 2025 as a SLSN-I at redshift $z \approx 0.072$ (ref. 11). On the basis of the redshift and assuming flat cosmological parameters ($\Omega_M = 0.286$, $\Omega_\lambda = 0.714$, $H_0 = 69.6$ km s^{-1} Mpc^{-1}), we use a distance of 327 Mpc to the SN. The host galaxy was exceptionally faint in our images and SN 2024afav is greatly offset from the centre (about 5′). Using the Na I D doublet method of ref. 48, we constrain the extinction owing to the host to be $E(B-V)_H \lesssim 0.04$ mag. However, on the basis of the line-of-sight extinction map[49], we correct photometry for a Milky Way extinction coefficient of $E(B-V)_{MW} = 0.0527 \pm 0.0029$ mag. We review the properties of instruments used in our campaign in Supplementary Information Section 1.

As observations were continuing, we predicted that our model would have a regime of validity bounded on the left by the diffusion timescale t_d and bounded on the right by the transition of the ejecta to the nebular phase. The magnetar+LT model assumes a luminosity driven by the magnetar wind interacting with the ejecta (Methods section 'Construction and fit of the Lense–Thirring modulation model'). Once the ejecta expand to the point at which they are no longer optically thick (indicated by a transition to the nebular phase, visible in the spectra, for example), this assumption (and therefore the model) is no longer applicable. Around the time the spectra transitioned to the nebular phase, we also observed a notable deviation from a luminosity power law $L(t) \propto (1 + t/t_p)^{-2}$ predicted by magnetar models (Extended Data Fig. 4), adding supporting evidence that the ejecta are no longer sufficiently optically thick to be illuminated by the magnetar wind. For these reasons, we constrain the regime of validity of our analysis to 37 days $\lesssim t \lesssim$ 181 days.

Magnetar-only model fits

The unusually bright light curve (about −20.5 peak absolute magnitude) with a long rise (>40 days; Methods section 'Observations and data reduction') are consistent with predictions for a SN explosion powered by a magnetar central engine, as described by the model of ref. 4. The magnetar model monotonically declines post-peak and is not expected to explain the chirped modulations. Despite this, the overall behaviour of the light curve may still be used to infer parameters of the magnetar system. We fit the magnetar model of ref. 4 to the entire dataset using the Modular Open Source Fitter for Transients (MOSFiT[50]), which has been used to fit a wide variety of SLSN-I light curves (for example, refs. 51,52). We initialize the fit with 1,600 walkers and use sufficient steps (about 8,000 after an approximately 2,000-step burn-in) to achieve convergence, which we measure through chain autocorrelation length and the improved Gelman–Rubin statistic, following Section 5.4 of ref. 53. The model includes a parameter (σ, units of mag) that scales the uncertainties so that the reduced χ^2 of the fit is approximately unity. Once convergence was achieved, parameter estimates and uncertainties were estimated by computing the highest posterior density interval around the maximum a posteriori value.

The results of the fit are shown in Extended Data Fig. 2. All fit-parameter posteriors were unimodal with approximately symmetric uncertainties. The fit explains the rise, peak and average decline well but, as expected, does not explain the modulations. The MOSFiT fit infers the presence of a magnetar with magnetic-field strength $B = (1.62 \pm 0.1) \times 10^{14}$ G and spin period $P_{spin} = 4.19 \pm 0.18$ ms, illuminating ejecta of mass $M_{ej} = 10 \pm 1.1\ M_\odot$ expanding with velocity $(5.754 \pm 0.12) \times 10^3$ km s^{-1}. The magnetar properties are consistent with expectations from theory[4] and surveys of other SLSNe-I (refs. 51,52), as shown in Extended Data Fig. 5.

We consider the possibility that the bumps may be substantially altering the outcome of the fit, as the largest modulations represent ±1-mag deviations from the magnetar model. To address this, we re-perform the magnetar fit, using only data from $\lesssim$50 days (approximately the diffusion timescale). We find that fitting using this reduced sample of the data moderately affects the best-fit parameters. First, the uncertainties substantially increase across all parameters owing to the lack of data, as only Asteroid Terrestrial-impact Last Alert System (ATLAS) *c*-band and *o*-band data were consistently available before peak brightness (Methods section 'Observations and data reduction'). The period is statistically consistent with the previous fit ($P_{spin} = 5.49^{+0.11}_{-1.25}$ ms). The magnetic-field strength and ejecta mass decrease substantially ($B = (1.0 \pm 0.7) \times 10^{14}$ G and $M_{ej} = 5.0^{+1.0}_{-4.7}\ M_\odot$). The ejecta velocity is again consistent with the previous fit and predictions from ref. 4 at $v_{ej} = 6.03^{+1.51}_{-2.75} \times 10^3$ km s^{-1}. In both fits, the behaviour of the light curve through the modulations is very similar, indicating that the bumps are not markedly affecting the post-peak behaviour of the model. However, the start of the modulations coincides approximately with the peak brightness of the SN, which is highly constraining for certain parameters (particularly the spin period, magnetic-field strength and diffusion timescale). By trimming our dataset to before the modulations began, we also limited the ability of the fit to properly constrain the peak of the light curve, possibly exacerbating discrepancies in the parameters between the two fits.

Residual analysis

We characterize the modulations by computing the residual between the data and the model fit in Methods section 'Magnetar-only model fits'. We work in magnitude space and weight all filters equally as (1) the behaviour is consistent enough in all bands to make this effective and (2) the spectral energy distribution of the object is complicated based on the spectra, which introduces uncertainty into (for example) a black-body fit to convert to luminosity space. The effect of this assumption is to make use of a flat spectral energy distribution, which is sufficient for our analysis but introduces minor deviations in some bands, as seen in Fig. 1. The result of this residual and subsequent binning is shown in Extended Data Fig. 3. We use a standard peak-extraction algorithm[54] to identify candidate extrema in each band, which we then aggregate by computing a mean location for each cluster of extrema weighted by the number of bands in which the extremum appears. Using this approach, we identify troughs at t = 65.3, 117.6, 139.9 and 160.4 days and peaks at t = 44.9, 93.6, 128.9 and 153.3 days, as well as a low-confidence peak detection at t = 168.8 days (see also Extended Data Table 1). Note that 'peak' and 'trough' refer to the conventional 'brighter' and 'dimmer' points on the light-curve residual, which are smaller and larger magnitude, respectively, owing to the construction of magnitudes. To quantify our confidence in the presence of the bumps, we fit a simple Gaussian model to each modulation and use the goodness of fit compared with a no-signal-noise model to compute the probability of false alarm (P_{FA}). We find that P_{FA} is $\ll$0.1% for all except the last two modulations. The penultimate dip (modulation 7) has a false-alarm probability of about 6%, which is acceptable. By contrast, the final modulations (8 and 9) have a P_{FA} of about 40%. Such a high false-alarm probability suggests that the final peak and dip are consistent with noise and not a robust detection. However, this quantitative metric substantially strengthens the evidence for the presence and location of the remaining bumps.

On the basis of the high-confidence peaks and troughs present, we compute a characteristic period (median of the set of computed periods) and period derivative for the residual modulations. To be conservative, we also exclude the first modulation at $t \approx 40$ days, as this may be degenerate with the magnetar-model peak. Using the peak-to-peak and dip-to-dip locations to estimate periods as a function of time, we fit a linear period variation (demonstrated in Extended Data Fig. 6) and find $P_c = 23 \pm 1.6$ days and a period derivative of $\dot{P}_c = -0.44 \pm 0.05$.

Uncertainties are based on errors in the peak locations, estimated by fitting a quadratic function to the local region around each extrema. We note that the choice of characteristic period and derivative estimation method does not greatly affect the results, as long as the corresponding period and period derivative are computed identically for the theoretical models.

Next we investigate the sinusoidal behaviour of the modulations and attempt to describe them phenomenologically. We construct a generic model to describe a sinusoid with varying periodicity and amplitude using

$$\Delta L(t) = \left[\sum_{a=0}^{n_a} c_a t^a\right] \cos\left[\sum_{p=0}^{n_p} c_p t^p\right], \quad (1)$$

which varies the periodicity and envelope using polynomials of arbitrary degree. We find that a quadratic ($n_a = 2$) polynomial envelope and a cubic ($n_p = 3$) phase function are required to describe the data to reduced $\chi^2 \approx 1$. The resulting fit (visualized in Extended Data Fig. 3) does not reproduce the very first modulation but produces peaks and troughs consistent with the remaining bumps. We use this phenomenological model to quantify our confidence in the presence of a chirp in the light curve. We compute the statistical significance of the model parameters from both $\Delta L = 0$ (no modulations) and $\phi(t) \propto t$ (linear phase indicating no chirp). Using likelihood-ratio tests ($\Delta\chi^2$) against nested null models, we find that both the pure-noise and constant-periodicity hypotheses are rejected at $\gg 5\sigma$. We repeat this test with the fifth bump excluded and find the same results.

To further investigate the presence of a chirp in the light curve, we compute a power-density spectrum from the residuals from $t = 30$ to $t = 180$ days following ref. 55 and compare this spectrum with a simulated static-period signal as well as a simulated chirp (contaminated with noise comparable with the SN 2024afav light curve). The results of this comparison are shown in Extended Data Fig. 7. A static period will produce a narrow peak at a single frequency but the presence of a chirp characteristically 'smears' the highest-amplitude frequencies. We confirm that the SN 2024afav light curve indeed produces a power-density spectrum profile characteristic of a chirp and visibly inconsistent with a static period. Together, the above evidence indicates the presence of four robust modulations with a clearly decreasing period. Further, the success of the phenomenological description of an envelope multiplied by a chirped sinusoid motivates our use of such a model to explore physical mechanisms, replacing the arbitrary phase function with a model-dependent one.

Construction and fit of the Lense–Thirring modulation model

To describe the fluctuations, we modify our phenomenological model (Methods section 'Residual analysis'), which can embed a chirped signal in a declining magnetar light curve. By replacing the arbitrary phase function in equation (1) with a physically motivated, model-dependent one, we may explore how the timings associated with different physical mechanisms compare with the observations.

We review the model presented in the main text, emphasizing that we cannot present a definitive model without theoretical investigation that is beyond the scope of this paper nor can we conclusively constrain all aspects of the energy injection scenario without further data. However, we may consider plausible physical mechanisms that can lead to a chirped light curve.

In the minutes to hours following core collapse and the magnetar birth, an accretion disk composed of fallback material from the progenitor envelope forms and circularizes[14,16,56,57]. The inner radius of the disk is suspended by a wind launched from the magnetar[17,18] or, in more extreme cases, the magnetosphere itself. Through some process during formation, the accretion disk becomes tilted or warped, perhaps because of the presence of a binary companion[58], a natal kick[59] or magnetic torques[36]. The tilted disk will experience a Lense–Thirring torque, inducing a precession around the spin axis of the magnetar[19,58]. The modulation of the magnetar signal by the accretion disk could occur in several ways. These include (but are not limited to) reflecting and obscuring the luminosity from the magnetar (as in, for example, refs. 24,25), jet redirection[26,27] along the normal of the plane of the accretion disk (as in, for example, ref. 28), wind redirection originating in the disk (as in, for example, ref. 29) or modulating the accretion rate onto the magnetar itself[30]. The proposed methods produce an anisotropic energy injection into the ejecta[24,25], which evolves owing to the precession of the disk and results in a modulated luminosity as seen by a distant observer[60,61]. Substantial theoretical investigation into each of these scenarios will be conducted in future work but is outside the scope of this analysis.

The torques induced in the disk by Lense–Thirring precession are communicated through the disk by viscous forces. In the inner disk, in which Lense–Thirring torques are the strongest, viscous torques may be insufficient to transport angular momentum quickly enough to prevent the shearing of the disk into distinct rings. Indeed, various groups have found that Lense–Thirring torques can lead to disk breaking within several tens of gravitational radii (for example, refs. 30,62–64). Reference 30 equated the viscous and Lense–Thirring torques to show that breaking occurs within a radius $R_{\rm break}$. Our best-fit parameters give an $R_{\rm break}$ value comparable with the radius of the magnetar—two orders of magnitude below that of the light cylinder—indicating that the disk is unaffected by warping or breaking owing to Lense–Thirring torques. A break radius comparable with the light cylinder would require a disk aspect ratio $H/R \lesssim 10^{-4}$, all else being equal, which is inconsistent with our fits of the disk properties (Supplementary Information Section 2). Thus, the Lense–Thirring torque is likely to dominate and drive the precession and therefore the modulations in the light curve. Although the magnetar exerts a torque on the accretion disk, we do not expect the accretion disk to affect the evolution of the magnetar. First, the inner radius of the accretion disk (set by $r_{\rm w}(t)$; Supplementary Information Section 2) is always outside the light cylinder of the magnetar ($R_{\rm LC} = cP/(2\pi) \approx 10^7$ cm $\ll r_{\rm w}$). More rigorously, Tong et al.[65] found that magnetars with surface-dipole strength $B \approx 10^{14}$ G or less do not have a notable impact on the evolution of their host magnetar, regardless of disk mass. As we are in this regime (Methods section 'Magnetar-only model fits'), we do not expect the accretion disk to have any impact on the magnetar and thus neglect this in our model.

Furthermore, to assume that the disk precesses as a solid body, we implicitly assume that $H/R \gtrsim \alpha$ (ref. 66). This assumption is consistent with the model we are invoking, as a relatively thick disk would be required to meaningfully occlude line-of-sight emission from the magnetar. Furthermore, we validate this assumption by checking that best-fit solutions for α satisfy this assumption, based on the computed radial evolution (Supplementary Information Section 2) and the standard α-disk prescription, following ref. 67 and using relationships summarized in ref. 56.

Finally, because the energy originates within an expanding SN ejecta, the observed light curve is greatly affected by the diffusion timescale $t_{\rm d}$ of the ejecta. References 7,8 found that, even after the diffusion timescale, modulations with timescales $\lesssim t_{\rm d}$ are smoothed out but modulations that occur with characteristic timescale $> t_{\rm d}$ will be phase shifted. For an expanding ejecta with $M \approx 7.5\,M_\odot$ and velocity $v \approx 6 \times 10^3$ km s^{-1}, the timescale at $t \approx 80$ days is $t_{\rm d} \approx 30$ days (versus the observed period of about 50 days, ratio approximately $1.6 > 1$). Towards the end of the modulations, the diffusion timescale at $t \approx 150$ days is $t_{\rm d} \approx 15$ days (versus the observed period of about 20 days, ratio approximately 1.3). Physical mechanisms producing periodic modulations on a shorter timescale than $t_{\rm d}$ may result in approximately sinusoidal oscillations as the finer structure is smoothed out[34]. The primary effect of the diffusion timescale, then, is to delay the emission by $t_{\rm d}(t)$. We account for this by correcting the peak locations by about $t_{\rm d}$ before attempting to reproduce the periodicity in the extrema-only calculations (Supplementary Information Section 2). We find that the results are not highly sensitive to the magnitude of

this correction; we could obtain acceptable results even just assuming a constant diffusion offset equal to the average $t_d(t)$ between 80 and 160 days. In the full light-curve fit, this average offset is absorbed into the ϕ_0 parameter. The light-curve modulations also seem to vary in amplitude; the physical origin of the amplitude modulation in the residual is uncertain. Plausible interpretations will vary depending on the specific assumption of anisotropic emission generator; for example, a jet-based model may see amplitude fluctuation owing to the variation of the jet power, whereas a disk-wind-based model may see variation owing to changes in disk size with time. Future investigation into energy-injection scenarios will require substantial theoretical work outside the scope of this analysis but yield quantitative predictions for the residual amplitude behaviour, helping constrain the underlying mechanism.

Modulation reproduction with magnetar parameters. The extra signal in the light curve is well approximated as the cosine of a phase function, as motivated by the analysis of the residuals (Methods section 'Residual analysis'). For our model, we assume that the frequency is driven by Lense–Thirring precession and derive an approximate phase function for the disk in Supplementary Information Section 2. The phase function is determined by the magnetar properties, an accretion rate and an overall offset. By considering only the locations of the peaks of the modulations corrected for the instantaneous diffusion timescale, we can fit the phase function directly without the rest of the light curve or describing the envelope. In this way, we can directly examine the parameters of the magnetar, independent from the rest of the light curve. We perform this fit with disk outer–inner radius ratio $r_o/r_i = 25$, allowing the magnetic-field strength, α-disk parameter, accretion rate and period to vary. We find $\alpha = 0.07 \pm 0.03$ and constrain the accretion rate through the disk at $t = 30$ days to be $\dot{M}_0 = (3.71 \pm 0.36) \times 10^{-5}\ M_\odot$ per year. This value is correlated with the choice of r_o/r_i, which introduces an extra source of uncertainty. We find that varying r_o/r_i between 1 and 30 varies the accretion rate by roughly $(1.6 \pm 10^{-5})\ M_\odot$ per year but without a meaningful constraint as r_o/r_i is almost completely degenerate with $\dot{M}_0$. When the accretion rate is allowed to vary to balance the change in r_o/r_i, we find that the resulting best-fit P_c and $\dot{P}_c$ change by $\lesssim$4% and $\lesssim$6%, respectively. This consistency validates our simplifying assumption of constant r_o/r_i; even if this ratio varies because of spreading or infall, our testing indicates that the resulting inferred P_c and $\dot{P}_c$ will not be substantially altered. Notably, we also find that the magnetic-field strength is well constrained to $B = (1.9 \pm 0.6) \times 10^{14}$ G, consistent with the values from the bumpless fits in Methods section 'Magnetar-only model fits'; similarly, we find $P_{spin} = 5.42^{+4.53}_{-1.81}$ ms, also consistent with the bumpless fits in Methods section 'Magnetar-only model fits'. The resulting agreement across disjoint observables eliminates degeneracy with external power sources (CSM interaction, flares and so on) and rules out coincidental tuning of free parameters: single B and P_{spin} values reproduce both the modulation evolution and the total luminosity evolution. Such a result unifies timing and energetics under one physical engine.

We combine a Gaussian envelope (motivated by the shape of the modulation amplitude in the residuals; Methods section 'Residual analysis') and the phase function in Supplementary Information Section 2 to form an overall fit function,

$$\Delta L(t) = \left(A_0 \exp\left[-\left(\frac{t - t_{peak}}{A_1}\right)^2\right]\right) \times \cos\left[-\frac{7}{5}(r_o/r_i)^{-7/4}\frac{1-(r_o/r_i)^{7/4}}{1-(r_o/r_i)^{5/4}}\frac{GJ}{\dot{r}_i^3 c^2}(t_{infall}-t)^{-2} - \phi_0\right]. \quad (2)$$

This function has the following free parameters: A_0, setting the overall scale of the modulations; t_{peak}, setting the location of the envelope peak; A_1, setting the rise and decay of the envelope; $\dot{M}_0$ (the accretion rate through the disk at $t = 30$ days), which sets $\dot{r}$ and t_{infall}; and ϕ_0, which is an initial condition on the angle of the disk. In contrast to the self-consistency check performed in Supplementary Information Section 2, we fix all parameters that overlap with the MOSFiT magnetar model to those values identified in Methods section 'Magnetar-only model fits'. Finally, we incorporate a diffusion-timescale correction based on the optical depth of the expanding ejecta following ref. 34, motivated by previous studies, which found that anisotropies in input energy could propagate through the ejecta, resulting in viewing-angle-dependent light curves[60,61]. This correction washes out variability at early times when the diffusion timescale $t_d \gg t$ and results in a delay at later times when $t_d \lesssim 2\pi/\Omega_{LT}$. The delay is absorbed into the ϕ_0 parameter.

The results of the fit are shown in Extended Data Fig. 8. The physics-incorporated model achieves a similar goodness of fit (reduced $\chi^2 \approx 1.6$, number of data points $N = 618$, model degrees of freedom $k = 3$) to the purely phenomenological model in Methods section 'Residual analysis'. Reincorporating the model into the overall light curve as done in Fig. 1 emphasizes the ability of the model to explain the overall light curve and modulation behaviour in conjunction with the magnetar model of ref. 4. We investigate the impact of the diffusion correction by attempting the fit with and without it; we find that without the diffusion correction reduced $\chi^2 \approx 1.9$; by contrast, the diffusion correction improves the goodness of fit by almost 20% without adding any more parameters. This behaviour has been presented as evidence supporting a central-engine origin in previous works (for example, ref. 7), as processes external to the ejecta would not require a diffusion correction.

Similarly to the polynomial evolution model of Methods section 'Residual analysis', the magnetar+LT model has difficulty reproducing the peak at $t \approx 45$ days but more successfully reproduces the trough at $t \approx 70$ days. Decomposing the model into the precession and envelope as shown in Extended Data Fig. 8, we can immediately see that the precession model accurately reproduces the position of each peak and trough observed in the data. The inconsistency in the full model possibly originates from the amplitude component, which is probably too simple to explain the evolution of the modulations. This peak is also consistent with the expected peak of the light curve based on the magnetar model with no modulations, resulting in a small degeneracy about whether the very first peak is a result of the precession, the spin-down of the magnetar or both. However, this does not affect interpretation; as demonstrated in Supplementary Information Section 2, all physical quantities of interest can be estimated by fitting the extrema of our model to the dates of extrema in the light curve, without requiring a description of the amplitudes at all. There is also an inconsistency of about 15–20 days between the location of the trough at $t \approx 65$ days; however, all of the other extrema are well modelled by the precession component. Incorporating estimates of the period and magnetic field from both the precession (Supplementary Information Section 2), early light curve (Methods section 'Magnetar-only model fits') and full light-curve evolution (forward-modelling the light curve with both the magnetar model (Extended Data Fig. 2) and the precession component (Extended Data Fig. 8) simultaneously included), we estimate $P = 4.2 \pm 0.2$ ms and $B = (1.6 \pm 0.1) \times 10^{14}$ G.

Data availability

The photometric and spectroscopic datasets analysed during the present study are available in the WISeREP online database (https://www.wiserep.org/object/27312).

Code availability

The code used to run parts of this analysis as well as sample walkers from MOSFiT are available on Github (https://github.com/jrfarah/24afav_analysis).

47. Hogg, D. W., Baldry, I. K., Blanton, M. R. & Eisenstein, D. J. The K correction. Preprint at https://arxiv.org/abs/astro-ph/0210394 (2002).
48. Poznanski, D., Prochaska, J. X. & Bloom, J. S. An empirical relation between sodium absorption and dust extinction. *Mon. Not. R. Astron. Soc.* **426**, 1465–1474 (2012).
49. Schlafly, E. F. & Finkbeiner, D. P. Measuring reddening with Sloan Digital Sky Survey stellar spectra and recalibrating SFD. *Astrophys. J.* **737**, 103 (2011).
50. Guillochon, J. et al. MOSFiT: Modular Open Source Fitter for Transients. *Astrophys. J. Suppl. Ser.* **236**, 6 (2018).
51. Nicholl, M., Guillochon, J. & Berger, E. The magnetar model for type I superluminous supernovae. I. Bayesian analysis of the full multicolor light-curve sample with MOSFiT. *Astrophys. J.* **850**, 55 (2017).
52. Gomez, S. The Type I superluminous supernova catalogue I: light-curve properties, models, and catalogue description. *Mon. Not. R. Astron. Soc.* **535**, 471–515 (2024).
53. Farah, J. R. et al. Shock-cooling constraints via early-time observations of the Type IIb SN 2022hnt. *Astrophys. J.* **984**, 60 (2025).
54. Virtanen, P. et al. SciPy 1.0: fundamental algorithms for scientific computing in Python. *Nat. Methods* **17**, 261–272 (2020).
55. Lomb, N. R. Least-squares frequency analysis of unequally spaced data. *Astrophys. Space Sci.* **39**, 447–462 (1976).
56. Frank, J., King, A. & Raine, D. J. *Accretion Power in Astrophysics* 3rd edn (Cambridge Univ. Press, 2002).
57. Stone, N. & Loeb, A. Observing Lense-Thirring precession in tidal disruption flares. *Phys. Rev. Lett.* **108**, 061302 (2012).
58. Fragile, P. C. & Liska, M. in *New Frontiers in GRMHD Simulations* (eds Bambi, C., Mizuno, Y., Shashank, S. & Yuan, F.) 361–387 (Springer, 2025).
59. Brandt, N. & Podsiadlowski, P. The effects of high-velocity supernova kicks on the orbital properties and sky distributions of neutron-star binaries. *Mon. Not. R. Astron. Soc.* **274**, 461–484 (1995).
60. Barnes, J. et al. A GRB and broad-lined Type Ic supernova from a single central engine. *Astrophys. J.* **860**, 38 (2018).
61. Li, Y.-F. et al. The effect of anisotropic energy injection on the ejecta emission. *Astrophys. J.* **976**, 113 (2024).
62. Raj, A., Nixon, C. J. & Doğan, S. Disk tearing: numerical investigation of warped disk instability. *Astrophys. J.* **909**, 81 (2021).
63. Liska, M., Musoke, G., West, A., Krawczynski, H. & Tchekhovskoy, A. GRMHD simulations of misaligned and truncated accretion disks. *Bull. Am. Astron. Soc.* https://baas.aas.org/pub/2022n3i110p91/release/1 (2022).
64. Musoke, G., Liska, M., Porth, O., van der Klis, M. & Ingram, A. Disc tearing leads to low and high frequency quasi-periodic oscillations in a GRMHD simulation of a thin accretion disc. *Mon. Not. R. Astron. Soc.* **518**, 1656–1671 (2023).
65. Tong, H., Wang, W., Liu, X. W. & Xu, R. X. Rotational evolution of magnetars in the presence of a fallback disk. *Astrophys. J.* **833**, 265 (2016).
66. Fragner, M. M. & Nelson, R. P. Evolution of warped and twisted accretion discs in close binary systems. *Astron. Astrophys.* **511**, A77 (2010).
67. Shakura, N. I. & Sunyaev, R. A. Black holes in binary systems. Observational appearance. *Astron. Astrophys.* **24**, 337–355 (1973).
68. Kendall, M. & Stuart, A. *The Advanced Theory of Statistics. Vol. 2: Inference and Relationship* (Hodder Arnold, 1979).

Acknowledgements We thank L. Bildsten, O. Blaes, S. Wong, J. Delgado, C. Fragile and D. Kasen for helpful discussions. J.R.F. is supported by the U.S. National Science Foundation (NSF) Graduate Research Fellowship Program under grant 2139319. This work makes use of data from the Las Cumbres Observatory (LCO) global telescope network. The LCO group is supported by NSF grants AST-1911225 and AST-1911151. We respectfully acknowledge the profound cultural significance and enduring reverence of the summit of Haleakalā to the indigenous Hawaiian community and we are grateful for the opportunity to study the heavens from this mountain. This research was supported in part by grant NSF PHY-2309135 to the Kavli Institute for Theoretical Physics (KITP). L.J.P. is supported by a grant from the NASA Astrophysics Theory Program (ATP-80NSSC22K0725). The Flatiron Institute is supported by the Simons Foundation. A.V.F. acknowledges financial support from the Christopher R. Redlich Fund and many other donors. This work is supported by the U.S. NSF under Cooperative Agreement PHY-2019786 (the NSF AI Institute for Artificial Intelligence and Fundamental Interactions, http://iaifi.org/.) This work has made use of data from the Asteroid Terrestrial-impact Last Alert System (ATLAS) project. The ATLAS project is primarily financed to search for near-Earth asteroids through NASA grants NN12AR55G, 80NSSC18K0284 and 80NSSC18K1575; by-products of the near-Earth object search include images and catalogues from the survey area. This work was partially financed by Kepler/K2 grant J1944/80NSSC19K0112 and HST GO-15889 and STFC grants ST/T000198/1 and ST/S006109/1. The ATLAS science products have been made possible through the contributions of the University of Hawaii Institute for Astronomy, the Queen's University Belfast, the Space Telescope Science Institute, the South African Astronomical Observatory and the Millennium Institute of Astrophysics (MAS), Chile.

Author contributions J.R.F. initiated the study and conceived the mechanism, helped organize follow-up observations of the object with the LCO, processed LCO photometry and spectra, performed the analysis and led the writing of the manuscript. L.J.P. assisted with the theoretical development of the mechanism and alternatives and contributed text to the manuscript. L.J.P., Y.Q.N. and D.A.H. contributed equally to development of the mechanism and application to observables. C.M., M.A., H.K., D.H., S.G., K.W., A.V.F., E.B. and P.B. provided data, assisted with interpretations and gave feedback on the manuscript. K.A.B. developed the lcogtsnpipe software that was used for reductions of LCO photometry.

Competing interests The authors declare no competing interests.

Additional information

Supplementary information The online version contains supplementary material available at https://doi.org/10.1038/s41586-026-10151-0.

Correspondence and requests for materials should be addressed to Joseph R. Farah.

Peer review information *Nature* thanks Adam Ingram and the other, anonymous, reviewer(s) for their contribution to the peer review of this work. Peer reviewer reports are available.

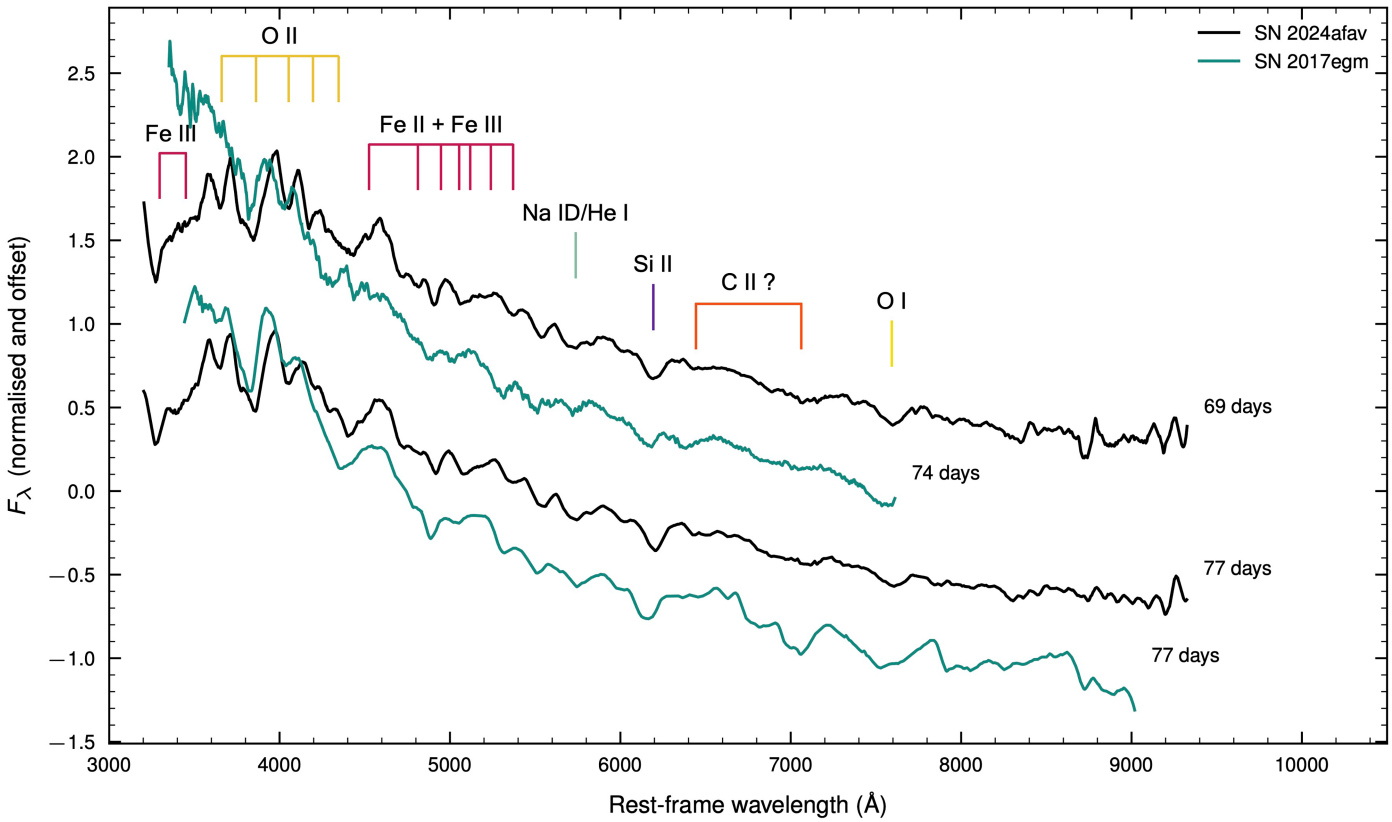

Extended Data Fig. 1 | Comparison of SLSN spectra. Comparison of the spectra of SN 2024afav (black) with the spectra of SN 2017egm (blue[41]), another well-known SLSN. Lines are shown at a velocity of about 8,000 km s^{-1}. The spectra of the two objects are similar, supporting the classification as a SLSN, to which the magnetar model of ref. 4 may be applicable. We note minor deviations from the spectra of SN 2017egm, such as variations in the strength of iron lines in the Fe II + Fe III complex around 5,000 Å. The spectral evolution of SN 2024afav is investigated in more detail in ref. 42.

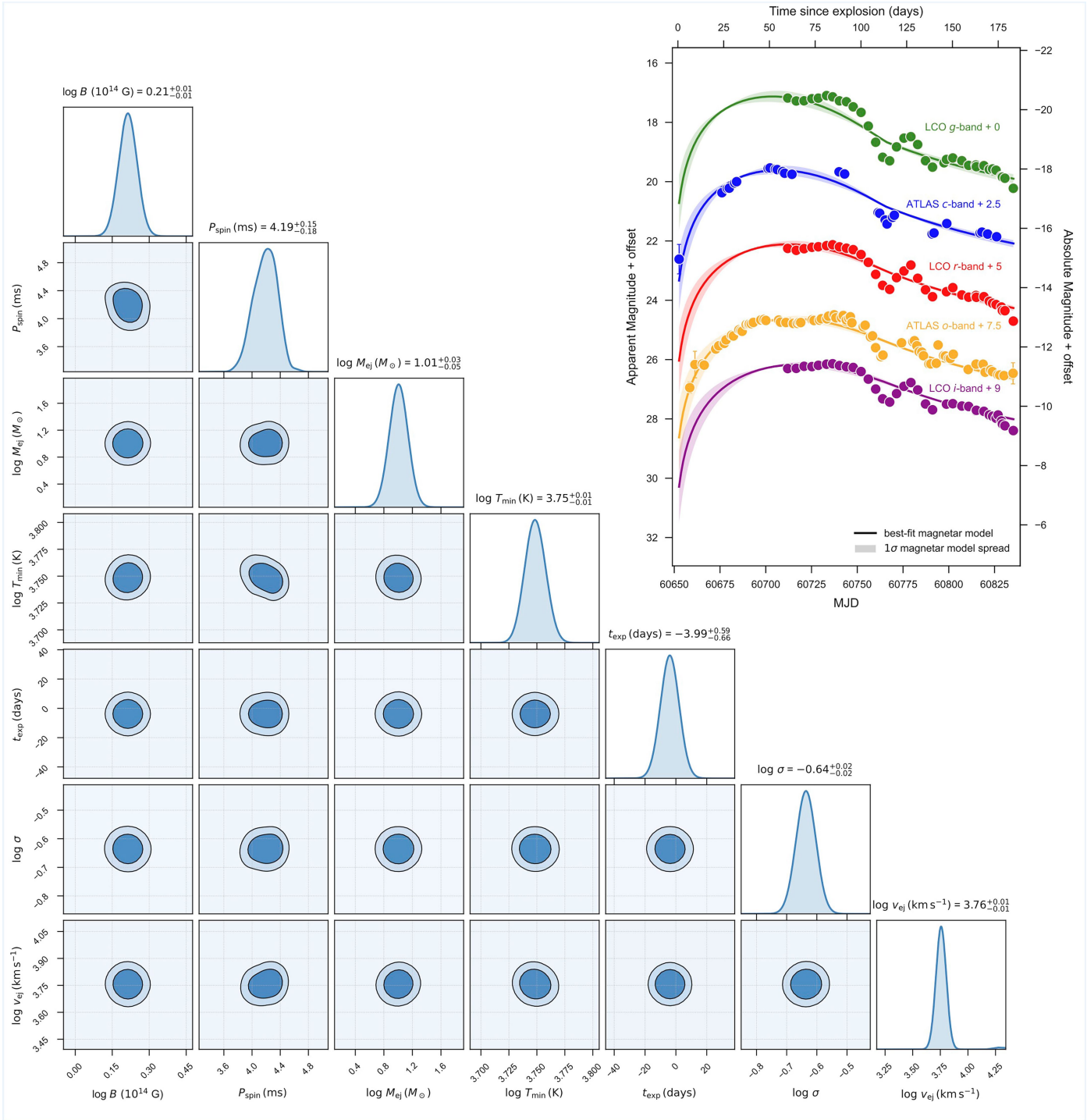

Extended Data Fig. 2 | Fit to the magnetar-only model. Corner plot and posterior samples (inset) for the magnetar-only model fit to the light curve of SN 2024afav. The σ parameter (units of mag) is an extra systematic uncertainty that the model is allowed to vary to bring the fit reduced χ^2 to 1. The posterior exploration achieved satisfactory convergence with minimal correlations between parameters and symmetric, unimodal uncertainties. The model explains the rise and overall trend of the light curve well; however, the model fails to explain the post-peak chirped modulations that appear in all bands. 1σ and 2σ regions of the joint posterior distributions are shown as contours.

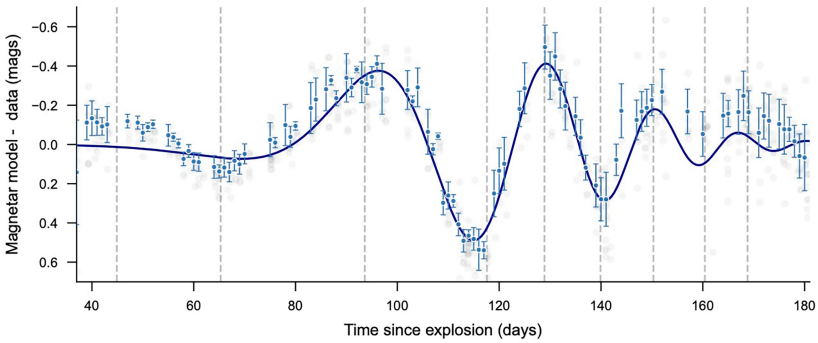

Extended Data Fig. 3 | Magnetar-model residuals. Residuals between the magnetar and model data across all bands phenomenologically investigated. The aggregated residuals from each band (grey points) are binned in time (blue points). Error bars represent the standard deviation of the photometry binned daily in all filters. We identify at least five clear bumps in the residual (grey dashed lines). To characterize the behaviour, we fit a combined quadratic polynomial envelope and a cubic polynomial phase function, for a total of seven free parameters (dark-blue line). The result of this fit indicates a hybrid growing/decaying envelope peaking around 120 days from the explosion epoch estimated by MOSFiT and a chirped signal with periodicity declining from $P \approx 50$ days to $P \approx 20$ days over the course of about 80 days. The fit underestimates the first peak but produces peaks consistent with the remaining modulations.

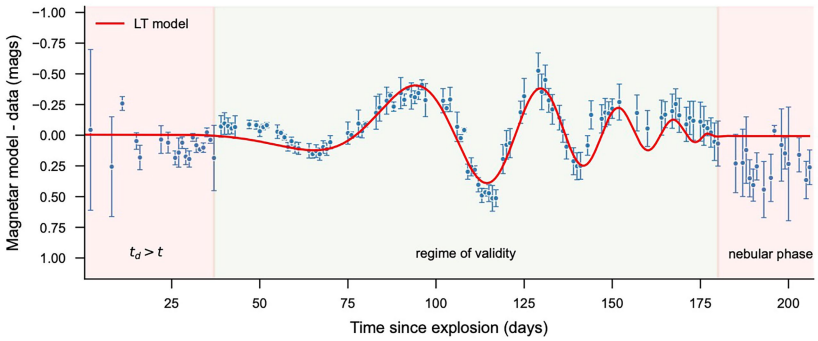

Extended Data Fig. 4 | Regime of validity of the LT model. Visualization of the regime of validity of the magnetar+LT model. Error bars represent the standard deviation of the photometry binned daily in all filters. The magnetar+LT model fundamentally assumes that the luminosity of the SN is driven by the emission interacting with the ejecta. At early times, when the diffusion timescale $t_d > t$, modulations are not visible and thus our model is not valid. At late times, when the ejecta are optically thin (nebular phase, indicated by the spectral evolution) and no longer illuminated by the magnetar wind, our model is similarly invalid. Between these two regimes, our model may be applied, as the ejecta are sufficiently optically thick to allow high-energy photons from the magnetar to be reprocessed but sufficiently optically thin to allow the reprocessed photons to escape.

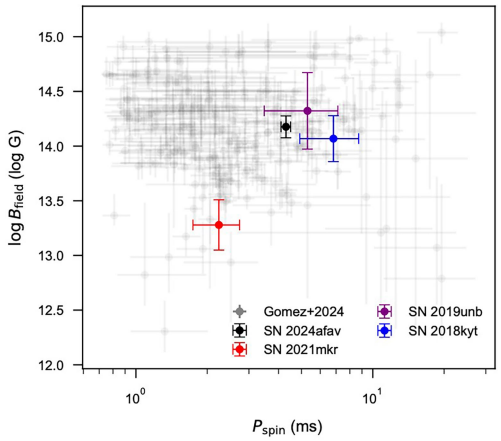

Extended Data Fig. 5 | Landscape of inferred magnetar properties in SLSNe-I. Comparison of P_{spin} and B_{field} between objects modelled with the magnetar+LT mechanism (SN 2024afav, SN 2021mkr, SN 2018kyt and SN 2019unb) and the sample of SLSNe-I provided in ref. 52. Error bars represent 1σ uncertainties on parameter estimates from the fits. The parameters inferred by our model are consistent with the overall distribution of SLSNe-I.

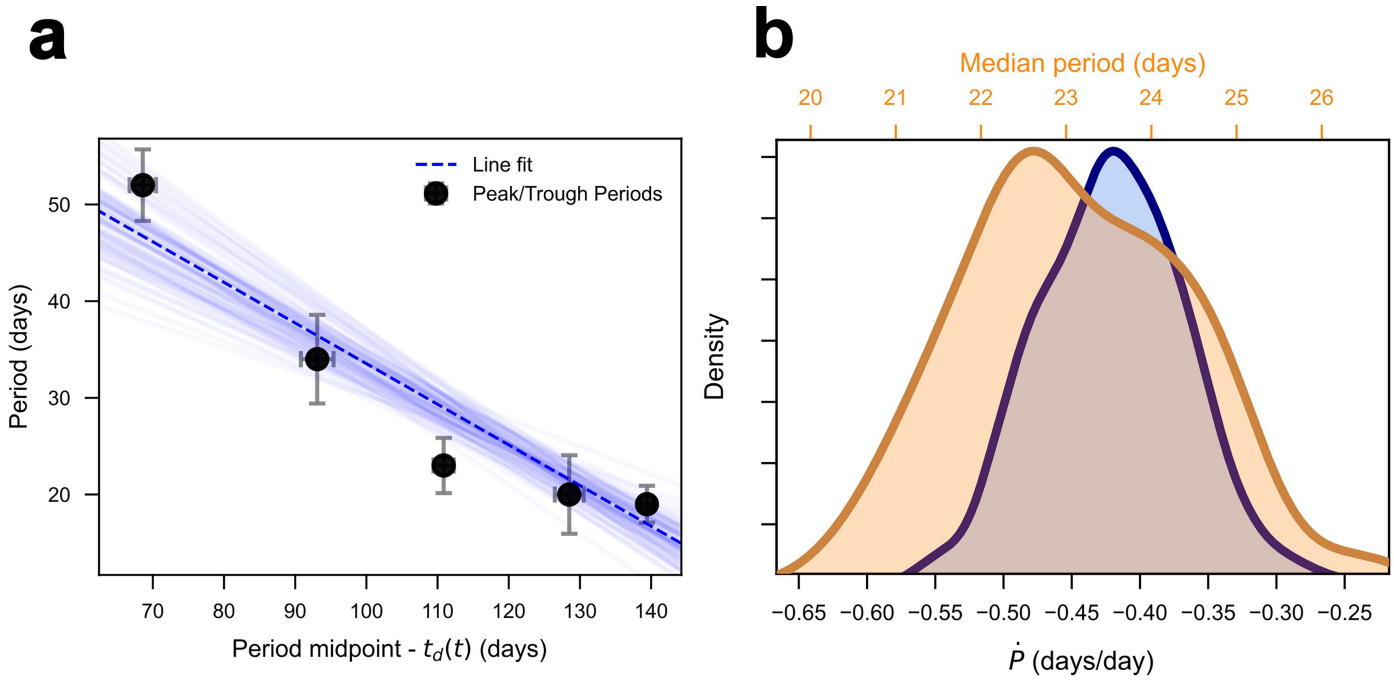

Extended Data Fig. 6 | Characteristic parameter estimation. We pedagogically demonstrate the procedure for estimating characteristic parameters $\dot{P}_c$ and P_c, as described in Methods section 'Residual analysis'. The left panel (**a**) shows the periods estimated from SN 2024afav, corrected for the diffusion timescale, with 1σ uncertainties propagated from quadratic fits to the modulations used to determine extrema positions. We fit a line to the periods and use a posterior sampling of the parameters to estimate the slope $\dot{P}_c = 0.44 \pm 0.05$ (right panel, **b**; blue distribution). Next we compute the median of the period measurements to get a characteristic period $P_c = 23 \pm 1.6$ days (uncertainty is estimated from the spread in the medians of the linear fits; right panel, **b**; orange distribution). For our models, which generate effectively continuous time series periods, we sample them on the same days as the period midpoints shown above and compute their characteristic quantities using that sampling. This serves as a pedagogical tool to help understand the ability of the models to describe the data.

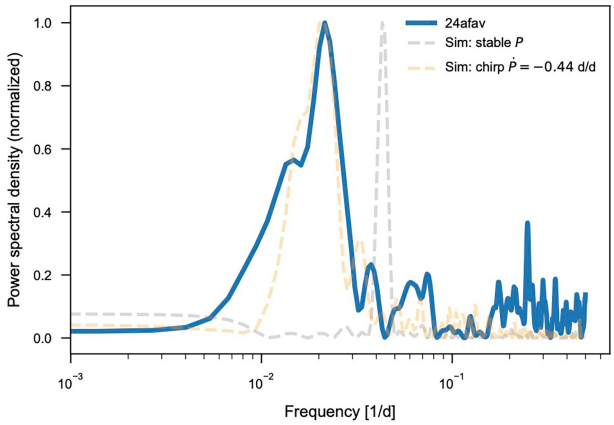

Extended Data Fig. 7 | Power spectral density of chirp. Power density spectrum of the SN 2024afav residual from $t = 30$ to $t = 180$ days in comparison with a simulated static period and a simulated chirp. The presence of the chirp 'smears' the peak frequency in a characteristic way, visible in both the simulated chirp and the SN 2024afav data. By contrast, a stable periodicity produces a narrow peak, which is clearly inconsistent with the SN 2024afav data.

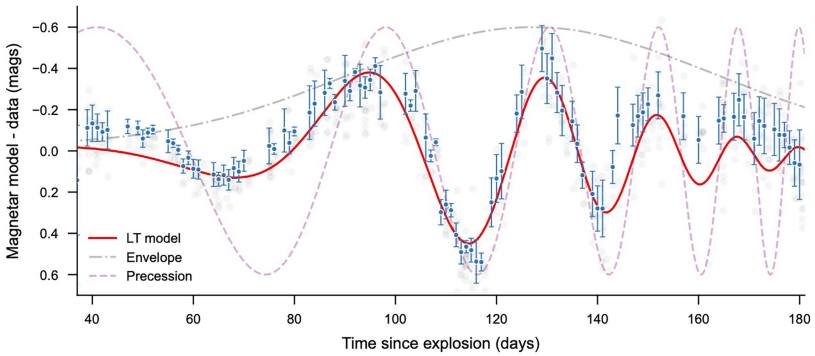

Extended Data Fig. 8 | LT model fit to residuals. Same as Extended Data Fig. 3 but instead investigated using the LT model. We characterize the residual behaviour using an amplitude envelope modulated by spin-down power and photon diffusion through the ejecta, combined with a precession governed by the Lense–Thirring effect. Unlike the seven-parameter phenomenological fit shown in Extended Data Fig. 3, this model only requires three parameters (overall scale, accretion rate and initial precession angle of the disk) yet explains the data to a similar degree of success. We show the decomposition of the model into the envelope and precession, which makes the shrinking period easily visible and demonstrates the consistency between the location of the four unambiguous bumps and the prediction from the Lense–Thirring effect.

Extended Data Table 1 | Modulation location and confidence

No.	Peak/dip?	t_{start}	t_{end}	Amplitude	P_{FA}
1	peak	35	60	0.43 ± 0.08	1×10^{-10}
2	trough	60	80	0.26 ± 0.04	1×10^{-7}
3	peak	80	110	0.47 ± 0.11	1×10^{-5}
4	trough	105	122	0.76 ± 0.04	6×10^{-4}
5	peak	122	136	0.49 ± 0.07	8×10^{-5}
6	trough	136	146	0.47 ± 0.03	2×10^{-7}
7	peak	146	154	0.34 ± 0.08	0.06
8	trough	154	166	0.14 ± 0.10	0.42
9	peak	166	175	0.18 ± 0.21	0.51

We compute the confidence of each modulation versus a null hypothesis of noise through a false-alarm probability P_{FA} (ref. 68) for bumps and dips. Start and end times of the modulations are approximate.